

Original research paper

## Passive acoustic monitoring of a natural CO<sub>2</sub> seep site – Implications for carbon capture and storage



Jianghui Li<sup>a,\*</sup>, Ben Roche<sup>b</sup>, Jonathan M. Bull<sup>b</sup>, Paul R. White<sup>a</sup>, John W. Davis<sup>b</sup>, Michele Deponte<sup>c</sup>, Emiliano Gordini<sup>c</sup>, Diego Cotterle<sup>c</sup>

<sup>a</sup> Institute of Sound and Vibration Research, University of Southampton, Southampton SO17 1BJ, UK

<sup>b</sup> Ocean and Earth Science, University of Southampton, National Oceanography Centre, Southampton SO14 3ZH, UK

<sup>c</sup> OGS - National Institute of Oceanography and Applied Geophysics, 34010 Sgonico, TS, Italy

### ARTICLE INFO

#### Keywords:

Bubble transect  
Underwater acoustics  
Multipath  
Greenhouse gas  
Marine carbon capture and storage

### ABSTRACT

Estimating the range at which an acoustic receiver can detect greenhouse gas (e.g., CO<sub>2</sub>) leakage from the sub-seabed is essential for determining whether passive acoustic techniques can be an effective environmental monitoring tool above marine carbon storage sites. Here we report results from a shallow water experiment completed offshore the island of Panarea, Sicily, at a natural CO<sub>2</sub> vent site, where the ability of passive acoustics to detect and quantify gas flux was determined at different distances. Cross-correlation methods determined the time of arrival for different travel paths which were confirmed by acoustic modelling. We develop an approach to quantify vent bubble size and gas flux. Inversion of the acoustic data was completed using the modelled impulse response to provide equivalent propagation ranges rather than physical ranges. The results show that our approach is capable of detecting a CO<sub>2</sub> bubble plume with a gas flux rate of 2.3 L/min at ranges of up to 8 m, and determining gas flux and bubble size accurately at ranges of up to 4 m in shallow water, where the bubble sound pressure is 10 dB above that of the ambient noise.

### 1. Introduction

In recent years, the storage of carbon dioxide (CO<sub>2</sub>) within sub-seabed reservoir has been discussed and identified as an important strategy to mitigate the increase in global temperature due to the increase in atmospheric CO<sub>2</sub> (Pachauri et al., 2014; Roelofse et al., 2019; Caserini et al., 2017; Vielstädte et al., 2019). Many studies have acknowledged that effective monitoring techniques for potential CO<sub>2</sub> gas seepage through the seabed, above carbon capture and storage (CCS) complexes, are essential (Loewen and Melville, 1991; Leighton and White, 2011; Blackford et al., 2015; Mabon et al., 2014; Hvidevold et al., 2016; Bergès et al., 2015; Atamanchuk et al., 2015; Taylor et al., 2015; Cevatoglu et al., 2015; Shitashima et al., 2015; Kolster et al., 2018; Stork et al., 2018; Kita et al., 2015). Gas bubbles within the seabed migrate, as a result of buoyancy, through a variety of possible pathways to the surface of the seafloor, where they escape into the overlying ocean (von Deimling et al., 2015). As the bubbles become entrained in the water they undergo volume oscillations which radiate sound into the environment (Strasberg, 1956) which can be used to detect and quantify the gas flux (Leighton and White, 2011). This paper explores the effectiveness of passive acoustic monitoring for sites above marine CCS storage reservoirs by completing an experiment

over a natural CO<sub>2</sub> seep offshore Panarea.

Marine monitoring strategies of CO<sub>2</sub> gas seeps using acoustics include time-lapse acoustic investigations using single/multi-beam echosounders (Blackford et al., 2015; Veloso et al., 2015) and horizontal backscattering solutions (Leblond et al., 2014). Active methods are well suited to detection of gas seepage, particularly for gases with low solubility, e.g., methane (CH<sub>4</sub>). While for gases possessing higher solubility, such as the CO<sub>2</sub>, the dimensions (height and width) of any emerging gas plume would be smaller, making the detection of leakage/seepage with an active acoustic approach more difficult. Further, accurate quantification using active methods requires the use of sonar(s) with a broad range of frequencies, typically in the kHz range for exciting mm-scale bubbles (Li et al., 2019c). An alternative approach is to adopt passive acoustic methods to investigate the gas seepage from subsea installations (Blackford et al., 2015; Bergès et al., 2015; Li et al., 2019a). The most common passive acoustic approach is to measure acoustic sound radiated from gas seeps at a reference point which is close to the leak location (Leighton and White, 2011; Bergès et al., 2015; Li et al., 2019b). However there has been relatively little work to determine the distances at which passive acoustics can detect bubbles emerging from the seabed, or determine at what offsets the inversion of the recorded signal yields accurate estimates of gas flux. There are usually

\* Corresponding author.

E-mail address: [j.li@soton.ac.uk](mailto:j.li@soton.ac.uk) (J. Li).

<https://doi.org/10.1016/j.ijggc.2019.102899>

Received 29 May 2019; Received in revised form 5 November 2019; Accepted 6 November 2019

Available online 06 December 2019

1750-5836/ © 2019 Elsevier Ltd. All rights reserved.

two ways of looking at the passive assessment of flux: (1) in the case of low flux rate, i.e., individual bubbles can be clearly identified based on their resonant frequency, we can use their frequency without the strength of emission; (2) in the case of high flux rate, i.e., individual bubbles cannot be clearly identified, then the sound spectrum is used. Here we investigate the higher flux rate case.

For gas flux determination, the sound pressure level of CO<sub>2</sub> bubbles emitted from the seeps can be measured directly using a hydrophone. Based on the measured pressure level and analysis of sound frequency spectrum, the size distribution and population of CO<sub>2</sub> bubbles emitted from the seafloor seeps can be estimated using passive acoustic inversion (Leighton and White, 2011; Bergès et al., 2015; Li et al., 2019b). Leighton and White (Leighton and White, 2011) used a spherical spreading law to determine the monitoring range and gas flux, which simplifies the channel acoustic propagation and is incapable of incorporating surface- and bottom-reflected arrivals, which may be particularly significant in shallow water. The effectiveness of passive acoustics for *in situ* monitoring may be reduced due to the dynamic ambient environment, anthropogenic noise, noise from marine organisms, and its deployment may be restricted due to channel obstacles, ocean dynamics (Leifer and MacDonald, 2003), acoustic attenuation, bathymetry, and multipath propagation (Li et al., 2016, 2018; Li, 2017; Li and Zakharov, 2018). Thus the low intensity sounds emitted by the bubbles relative to background ocean noise means that passive acoustic monitoring is usually conducted at distances close to gas seeps.

In this study, a field experiment was conducted using an acoustic recorder with multiple hydrophones deployed at various distances from a natural CO<sub>2</sub> gas seep, to investigate the effectiveness of passive acoustics for detecting and quantifying bubble sound arrivals as a function of range. An additional goal was to understand potential interference factors on bubble monitoring. In free space, the sound propagation can be considered as spherical spreading without reflection from channel boundaries. While

in an underwater acoustic channel, the sea surface and seabed may act as reflection boundaries; we call the length of the actual propagation path the channel equivalent range. To find the equivalent range for gas flux determination in shallow water, considering channel multipath and attenuation, we develop a model based on ray-tracing to match acoustic arrivals at each hydrophone location.

The CO<sub>2</sub> vent sites offshore Panarea, Italy are similar to possible leakage scenarios from sub-seabed reservoirs in shelf areas (Schmidt et al., 2015) albeit in waters which are shallower than those typical of sites proposed for marine CCS schemes. It provides an ideal natural laboratory (Kirk, 2011), for the investigation of CCS leakage detection and monitoring strategies. Here we describe the deployment of the acoustic recorder offshore Panarea and techniques as well as modelling used to process the acoustic data (Section 2). Then we report the results (Section 3) obtained from the deployment along a transect near a selected natural CO<sub>2</sub> gas seep. These field results, i.e., acoustic channel multipath structure, gas plume detection, gas flux and bubble size determination, are used to illustrate the potential of our passive acoustic approach for CCS gas leakage detection and quantification in real shallow water scenarios. We discuss the applicability of using the developed techniques in deeper water as one of the strategies for leakage monitoring of marine carbon storages sites in Section 4.

## 2. Materials and methods

### 2.1. Study site

Panarea, located in the southern Tyrrhenian Sea, is an island within the 200 km long Aeolian Arc, parallel to the continental slope of north coast of Sicily and western coast of Calabria (Li et al., 2019a; Schmidt et al., 2015; Lupton et al., 2011; Graziani et al., 2014; Caramanna et al., 2011, 2013; Beccaluva et al., 1985). Fig. 1 shows the Panarea and the

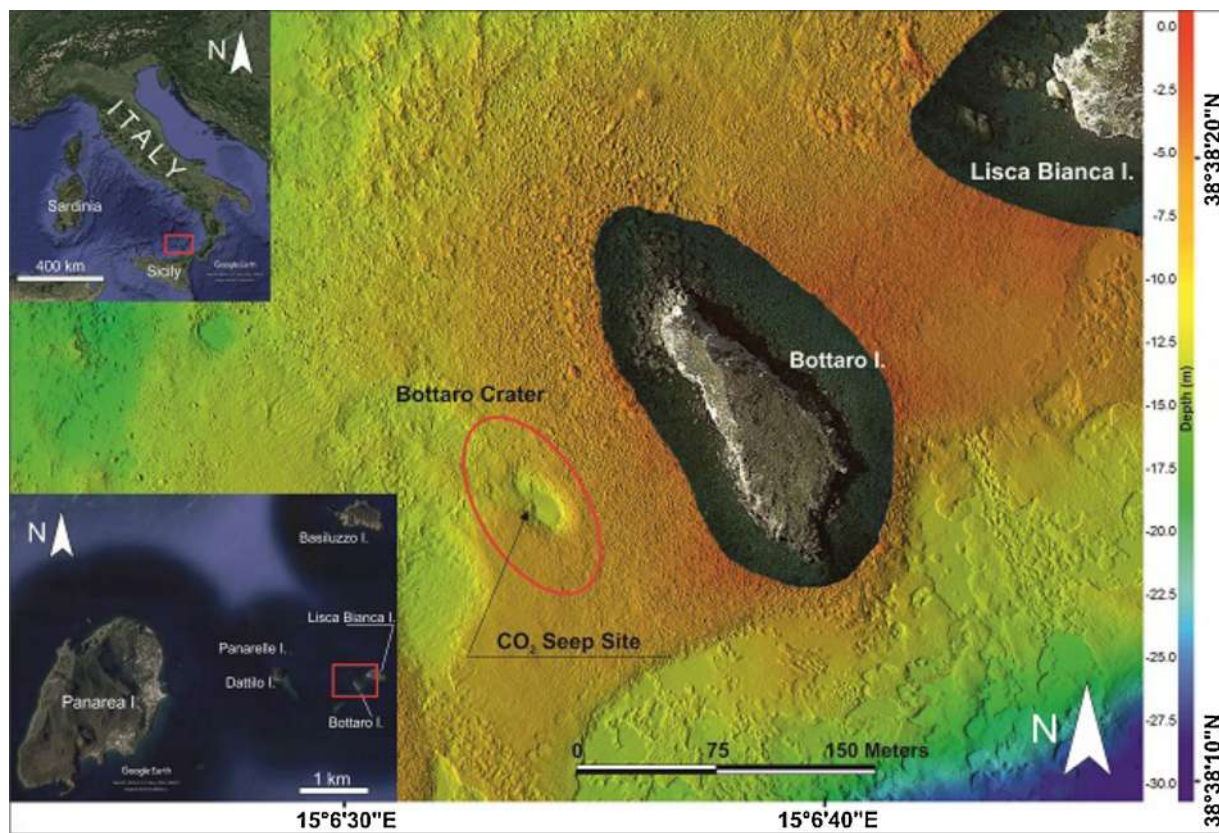


Fig. 1. Maps showing the position of the CO<sub>2</sub> seep site offshore Panarea (c. 100 m west of Bottaro Islet in 12.5 m water depth). The passive acoustic experiment investigated a seep site (a 10 cm wide pockmark) towards the edge of Bottaro Crater; the position of the Crater is shown by the red circle. (For interpretation of the references to colour in this figure legend, the reader is referred to the web version of this article.)

small islets situated to the east. The island and these islets are the emergent parts rising from the western section of a submarine stratovolcano (Schmidt et al., 2015; Dekov and Savelli, 2004; Esposito et al., 2006). The stratovolcano is over 1200 m in height (Gabbianelli et al., 1990) and 20 km in width (Lucchi et al., 2007). Many volcanic craters are visible on the seabed, and a complex fracture system has been imaged with an overall SW-NE orientation which may link Panarea with a nearby volcano island Stromboli in the northeast direction.

The islets east of Panarea are situated on a shallow plateau with water depth of 30 m (Graziani et al., 2014; Anzidei et al., 2005), where extensive fluid exhalations into the water column occur from the volcanic activity. Numerous gas leakages have been measured, with relatively stable composition of around 98% CO<sub>2</sub>, 1.7% H<sub>2</sub>S and other trace gases (N<sub>2</sub>, He, H<sub>2</sub>, CH<sub>4</sub>) (Caramanna et al., 2011; Aliani et al., 2010; Caracausi et al., 2005; Chiodini et al., 2006), while flux rates vary from different gas seeps. These natural gas release seeps and the CO<sub>2</sub>-rich gas composition make the area offshore Panarea an excellent test bed to study gas leakage scenarios and detection methods. Previous studies offshore Panarea have mapped (Italiano and Nuccio, 1991; Calanchi et al., 1995) the rising (CO<sub>2</sub> and CH<sub>4</sub>) gas plumes at 80 different locations (Schmidt et al., 2015); and continuous acoustic monitoring of bubble flux has been conducted (Italiano et al., 2011). However, there has been no investigation of the distances from a seep site at which gaseous CO<sub>2</sub> can be detected and/or quantified using passive acoustics.

In this study, a volcanic crater (Bottaro Crater) generates a number of continuous CO<sub>2</sub>-rich gas bubbles streams (Fig. 2(b)). We chose to investigate a seep in 12.5 m water depth close to the rim of the crater, with a minimum distance of 20 m to other comparable bubble streams, and designed an experimental geometry that ran perpendicular to the crater edge. As well as making acoustic measurements at different distances, we used a diver-controlled funnel to directly measure the gas flux. To measure the real size of the rising bubbles, we used high-quality underwater video equipment (SONY FDR-X3000 Action Camera, with UltraHD resolution 4K (3840 × 2160) at 30p).

## 2.2. Acoustic receiver deployment

Two hydrophones linked to an acoustic recorder (*RS ORCA*) measured the sound of bubbles emerging from the seabed at different ranges. These hydrophones were absolutely calibrated with receive sensitivity of  $-164.5$  dB re: 1 V/ $\mu$ Pa. A gain of 15 dB data was applied to each recording channel, and a sampling frequency of 96 kHz was used. Data presented here was collected on May 16th 2018 when winds were light, sea state < 2 on the Beaufort scale.

Fig. 2(a) shows the cartoon experimental geometry on the edge of Bottaro Crater. To reduce the effects of reflections from the seabed (Fig. 2(b)), each hydrophone was fixed on a securely positioned tripod

on the seafloor at a height of 0.75 m. In the experiment, one hydrophone closest to the seep location at 0.3 m was used as the reference hydrophone and remained at a fixed location, whilst the other hydrophone was moved to various ranges to form a transect. The different acoustic channels were synchronously recorded. Acoustic measurements were conducted at horizontal distances between 0.3 and 8 m away from the centre of the seep site.

## 2.3. Signal processing and modelling

The approach to the bubble detection and quantification is shown in the block diagram Fig. 3. Measured data from the reference hydrophone (0.3 m away from the centre of the seep) is cross-correlated with measured data from the other transect locations to determine the travel times and ray paths for the sound emitted by bubbles emerging from the seabed for gas plume detection. Prior to the quantification of the gas flux, ray trace modelling using the Bellhop Acoustics Toolbox (Porter, 2011) is completed to obtain the channel impulse response for each hydrophone location along the transect. The impulse response is compared and corrected for the multipath structure derived from the bubble detection. The equivalent range for each hydrophone location from the centre of the seep corresponding to the channel impulse response, is applied into the passive inversion model (Leighton and White, 2011) to compute the gas flux and bubble size distribution and bubble numbers, and then gas flux. After we obtain the bubble size distribution and bubble numbers, we transfer it into a bubble forward model to generate modelled hydrophone data for comparison with the measured hydrophone data.

### 2.3.1. Ray trace based modelling

Ray trace modelling was used to compute the transmission loss and channel impulse responses (Porter, 2011). The sea surface was calm during the experiment, thus we assume the sea surface as flat in the simulation. The simulation incorporates the bathymetry shown in Fig. 2(a), the sound speed profile (SSP) shown in Fig. 4(a), and a central frequency of 350 Hz. The depth of the bubble sound source is at 12.5 m, and the positions of the transect hydrophone are set according to the deployment locations shown in Fig. 2(a). The bubble is much smaller than the wavelength of the sound radiated so is well-characterised as an omni-directional acoustic source. The seabed composition is a mixture of sands and gravels (Fig. 2(b)), and we used an estimate of  $\sim 0.7$  dB per wavelength attenuation (Jackson and Richardson, 2007).

We first carry out multiple runs to determine the channel impulse responses and the time delay of each arrival at the hydrophone positions. The arrival structure from the model (i.e., channel impulse responses), corresponding to the multipath arrivals, are then compared with the delays computed from the cross-correlation between reference

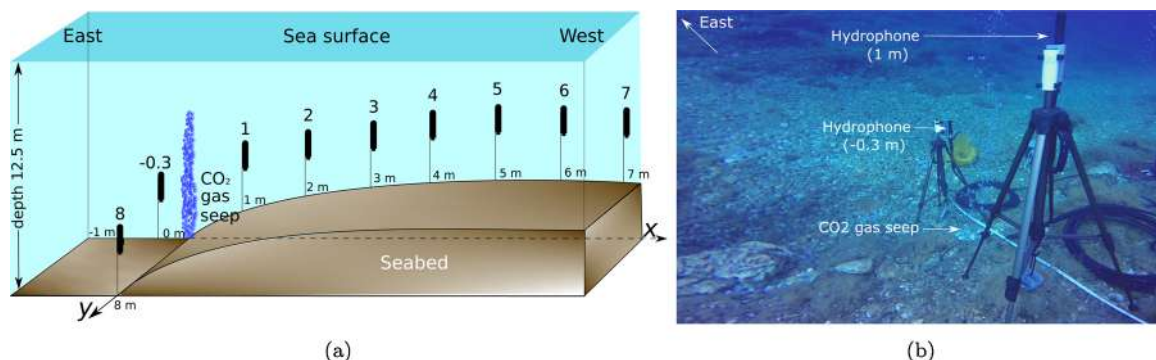
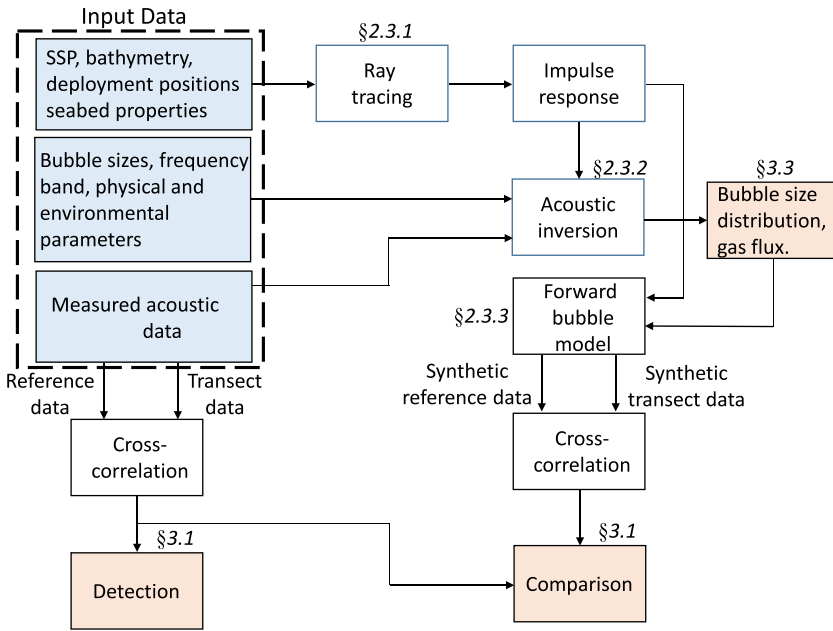


Fig. 2. Experimental geometry over natural CO<sub>2</sub> seep on the western edge of Bottaro Crater. (a) Overall experiment geometry showing the locations of the seep and hydrophone measurement positions. The transect was orientated east to west perpendicular to the edge of the crater. The seabed rose gently out of the crater to the west. An additional measurement was made at right angles to the transect at an offset of 8 m. (b) Underwater image of the central part of the experiment transects showing the reference hydrophone at 0.3 m and a transect hydrophone at 1 m from the seep.



**Fig. 3.** Block diagram of the approach to bubble/gas flux detection, quantification, and verification. Inputs are shown in blue colour, and outputs are shown in red colour. The steps are numbered corresponding to the paragraphs in the main text. For more details on the bubble passive inversion model see (Leighton and White, 2011; Bergès et al., 2015; Li et al., 2019b). (For interpretation of the references to colour in this figure legend, the reader is referred to the web version of this article.)

field data and transect field data. As the measured sound arrived via multiple paths, these results are used to compute the equivalent propagation range  $\hat{r}$ :

$$\hat{r} = \frac{r_0 \bar{A}_0}{\sum_{i=1}^I A_i}, \quad i = 1, \dots, I, \quad (1)$$

where  $r_0$  is the range of a reference point with sound signal arriving only from the direct path,  $\bar{A}_0$  is the path impulse amplitude received at the reference point,  $I$  is the number of multipath, and  $A_i$  is the amplitude of the path impulse response for each arrival, usually overlapped temporally in shallow water, considering reflection from sea surface and ocean bottom with phase shift.

### 2.3.2. Passive inversion model

For inversion of the gas flux from the bubble stream, we identify the frequency range,  $[f_{\min}, f_{\max}]$  over which the sound of the bubbles is evident above the ambient noise field. Ambient condition was measured well away from any seep site location. The radii of the bubbles whose resonant frequencies correspond to  $f_{\min}$  and  $f_{\max}$  are identified as  $R_{\max}$  and  $R_{\min}$  respectively (Leighton, 1994), according to the low-amplitude pulsations occur at a natural angular frequency  $\omega_0 (= 2\pi f)$ , which is given by (Leighton, 1994):

$$\omega_0 = \frac{1}{R_0 \sqrt{\rho_0}} \sqrt{3\kappa \left( p_0 - p_v + \frac{2\sigma}{R_0} \right) - \frac{2\sigma}{R_0} + p_v - \frac{4\eta^2}{\rho_0 R_0^2}}, \quad (2)$$

where  $R_0 \in [R_{\min}, R_{\max}]$  is the bubble equilibrium radius [m],  $\rho_0$  is the ambient liquid density [ $\text{kg}/\text{m}^3$ ],  $p_0$  is the ambient pressure [Pa],  $p_v$  is the vapour pressure [Pa],  $\sigma$  is the surface tension [ $\text{N}/\text{m}$ ],  $\eta$  is the shear viscosity [ $\text{Pa s}$ ], and  $\kappa$  is the ratio of specific heat of the gas at constant pressure to that at constant volume, depending on whether the gas is behaving adiabatically, isothermally, or in some intermediate manner (Siedler and Peters, 1986).

Then we create a bin vector of the radii  $R_0$  with a bin width of  $(R_{\max} - R_{\min})/M$ , where  $M$  is the number of bins. For each bin, we integrate the measured power spectral density (PSD) across the frequency range corresponding to the resonant frequencies of the radii in the bin (Leighton and White, 2011). The modelled spectrum of a single bubble emission is given by (Leighton and White, 2011):

$$|X_b(\omega; R_0)|^2 = 2 \left[ (\omega_0^2 R_0^3) \frac{\rho_0 R_{\varepsilon 0i}}{\hat{r} R_0} \right]^2 \times \left( \frac{4 [(\omega_0 \delta_{\text{tot}})^2 + 4\omega^2]}{[(\omega_0 \delta_{\text{tot}})^2 + 4(\omega - \omega_0)^2][(\omega_0 \delta_{\text{tot}})^2 + 4(\omega + \omega_0)^2]} \right), \quad (3)$$

where  $R_{\varepsilon 0i}/R_0$  is the initial amplitude of displacement of the bubble

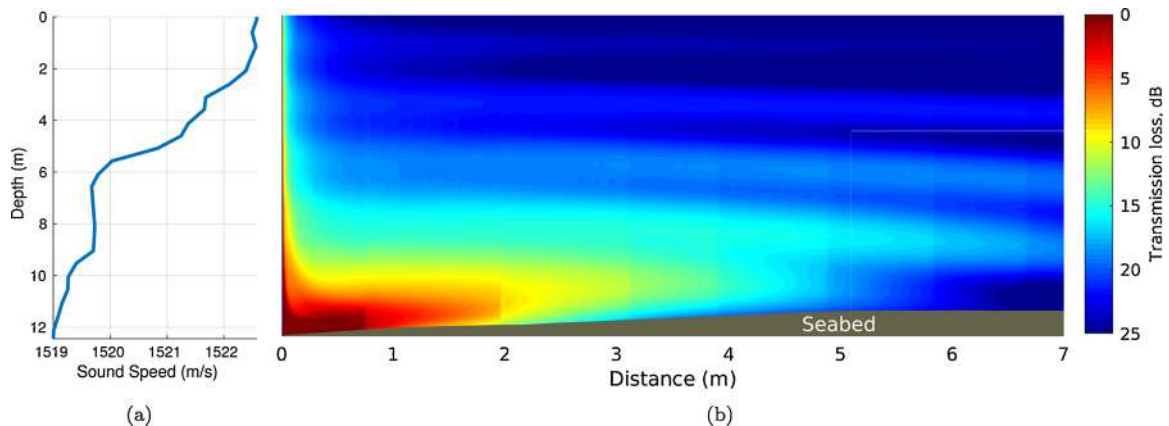


**Fig. 4.** Sound speed profile (SSP) collected on May 16th 2018 in the Panarea water area, and transmission loss within 7 m in the acoustic channel calculated using Bellhop. The seep site which is radiating bubble sounds is at a depth of 12.5 m. (a) Sound speed profile; (b) transmission loss structure at 350 Hz.

wall at the start of the emission as a proportion of the equilibrium bubble radius (see more details in Leighton and White (2011)). Here, we assume this ratio is constant to facilitate the inversion (Loewen and Melville, 1991).  $\delta_{tot}$  is the total dimensionless damping coefficient at bubble natural frequency (Leighton, 1994), and  $\hat{r}$  is the equivalent range computed from Eq. (1).

If the acoustic emissions of the bubbles are all uncorrelated, then the PSD  $S(\omega)$ , of the far-field acoustic signature of the bubble cloud can be expressed as

$$S(\omega) = \int_{R_0=R_{min}}^{R_0=R_{max}} D(R_0) |X_b(\omega; R_0)|^2 dR_0, \quad (4)$$

where  $D(R_0)$  is the bubble-emission size distribution as a function of the bubble radii  $R_0$ . Based on the computed acoustic pressure, we estimate the bubble size distribution and population from the recorded passive acoustic data, and solve Eq. (4) using the passive acoustic inverse method proposed by Leighton and White (2011). Thus, the probability density function (PDF) of bubble equilibrium radius  $p_b^{R_0}$  as well as number of bubbles for each size are obtained, and the gas flow rate  $F$  [L/min] is then computed as

$$F = \sum_{R_0=R_{min}}^{R_0=R_{max}} \frac{4}{3} \pi R_0^3 D(R_0). \quad (5)$$

Note that the pressure in the model (Leighton and White, 2011) is computed using spherical spreading, which is not applicable in shallow water channels where multipath effects should not be neglected. To make the inversion method applicable in shallow water, we use the equivalent range  $\hat{r}$  (Eq. (1)).

### 2.3.3. Forward modelling of bubble plume sound field

The inverted PDF of bubble equilibrium radius  $p_b^{R_0}$  and bubble numbers are used to generate a forward model. For a single bubble emitted from a seep, we assume the bubble oscillates in a limit of small amplitude  $|R_e| \ll R_0$ , which is valid for most ocean gas bubbles pulsating at their natural frequencies (Ainslie and Leighton, 2009). The oscillatory acoustic pressure signature in the liquid  $P_{b1}(t)$  of the monopole emission detected at time  $t$  by a hydrophone in the far field for a single pulsating bubble, is given by (Leighton and White, 2011):

$$P_{b1}^{R_0}(t, t_i) = (\omega_0 R_0)^2 \frac{\rho_0}{r_1} R_{e0} e^{-\omega_0 \delta_{tot}(t-t_i)/2} \times H(t - t_i) \cos \omega_0(t - t_i), \quad (6)$$

where  $t_i$  is the time at which the acoustic signal is first detected at the monitor,  $H$  is the Heaviside step function, and  $r_1$  is the reference range (1 m adopted here) from the bubble acoustic centre. Low-amplitude pulsations occur at a natural angular frequency  $\omega_0$ , which is given by Eq. (2) (Leighton, 1994).

If the acoustic emissions of the bubbles are all uncorrelated, then the far-field acoustic signature of the bubble cloud (gas flux) can be expressed as (Li et al., 2019b)

$$P_{b1}(t) = \sum_{i=1}^{N_b} P_{b1}^{R_0}(t, t_i), \quad t_i \in [0, T_b], \quad (7)$$

where  $t_i$  is randomly distributed in the interval  $[0, T_b]$ , following the bubble radius PDF  $p_b^{R_0}$ . Since we have now constructed time series of bubble singles, we convolve them with channel impulse responses and compute the reference/transect cross-correlation.

## 3. Results and discussion

At the seep site on the edge of Bottaro Crater, gas bubbles leaked from a seabed consisting of sands, gravels, and patches of sea grass (Fig. 2(b)). The  $CO_2$  emerged from a small circular pockmark of radius about 10 cm. The approach used to estimate the  $CO_2$  flux from the seep considers the acoustic data recorded at different distances together with

direct measurement of the flux. We determined how bubble sound propagates in the water column, then matched our modelling results to the field data, before determining the flux using the inversion approach. The SSP measured at the field site is shown in Fig. 4(a), and the modelled transmission loss (TL) structure using the SSP at 350 Hz (frequency peak of the measured bubble sound) is shown in Fig. 4(b), showing complex channel propagation and the TL structure.

### 3.1. Bubble sound field observations and arrival paths

For each distance of a hydrophone from the seep site, cross-correlation of the reference acoustic field data at  $-0.3$  m (sound predominantly from the gas seep) with the measured sound field was used to identify the major arrival paths (Fig. 5(a)) by matching with the impulse response derived from Bellhop ray-tracing modelling (Fig. 5(b), discussed in Section 3.3). The seep site bubble field is detected by the hydrophones from both the direct arrival and the water surface reflection at distances of 2–8 m. The direct path is well modelled (Fig. 5(b)) at all offset distances, while the water-surface reflection is best-modelled where the path amplitudes are the strongest (6 and 7 m).

The strength of the direct path signal decreases as the transect distance increases, and the normalised amplitudes show that the acoustic attenuation through direct propagation path is significant. Moreover, the direct path signal is greater than the reflected signal at distances up to 4 m, while the power strength of surface reflected path signal is greater than that of the direct ones at 6–7 m. At distances of 5 m and perpendicular 8 m the signals from the two paths are comparable where the Lloyd's mirror effect (discussed in Section 3.2) (Gerstein, 2002) is the strongest. As the transect distance increases, the delay for the direct path increases linearly, while the delay of reflected path does not.

To validate the multipath propagation along the transect, we estimated coordinates for each transect hydrophone from the delays for each path (direct/reflected) and compute the difference between physical length of the propagation path from the delays. Table 1 shows the results comparing the average delays calculated from cross-correlations and from measured positions of the hydrophones relative to the seep. It is seen that the error for each path calculation is less than 7%.

### 3.2. Spectral analysis

Continuous monitoring at a constant range from the seep site to the hydrophone yielded a concentrated interval of acoustic signal in the frequency domain, providing an initial frequency interval  $[f_{min}, f_{max}]$  for gas flux and bubble size determination. Fig. 6(a) shows the spectrogram from measured hydrophone data at  $-0.3$  m for 32 min. It is seen that the majority of the acoustic energy from the bubbles lies on a fairly broad frequency band 150–800 Hz, peaking at about 350 Hz.

Fig. 7 shows power spectral density (PSD) of the measured sound at ranges from  $-0.3$  to 4 m, and the ambient noise in this area without gas seeps observed. As the transect distance increases, the PSD of the measured sound decreases accordingly. Li et al. (2019b) concluded that for accurate field gas bubble sound detection and determination, the signal to noise ratio (SNR) should be at least 6 dB. In the shallow water case, where the effect from the sea surface and ambient are significant, the SNR should be higher than 6 dB, i.e., the PSD at 4 m is average  $\sim 10$  dB higher than that of the ambient noise in the frequency of interest (Fig. 7).

It should be noted that, as the transect distance increased from the seep site, constructive and destructive interference between the direct path and reflected path forms the Lloyd's mirror effect (Gerstein, 2002), plotted as dashed lines in Fig. 6(b) and dashed circles in Fig. 7. Such effect can cause significant interference on passive acoustic monitoring in shallow water, especially on the bubble size determination at low frequencies ( $< 500$  Hz), because sea surface sound reflections are nearly  $180^\circ$  out of phase with the direct sound arrivals. Bubble sounds

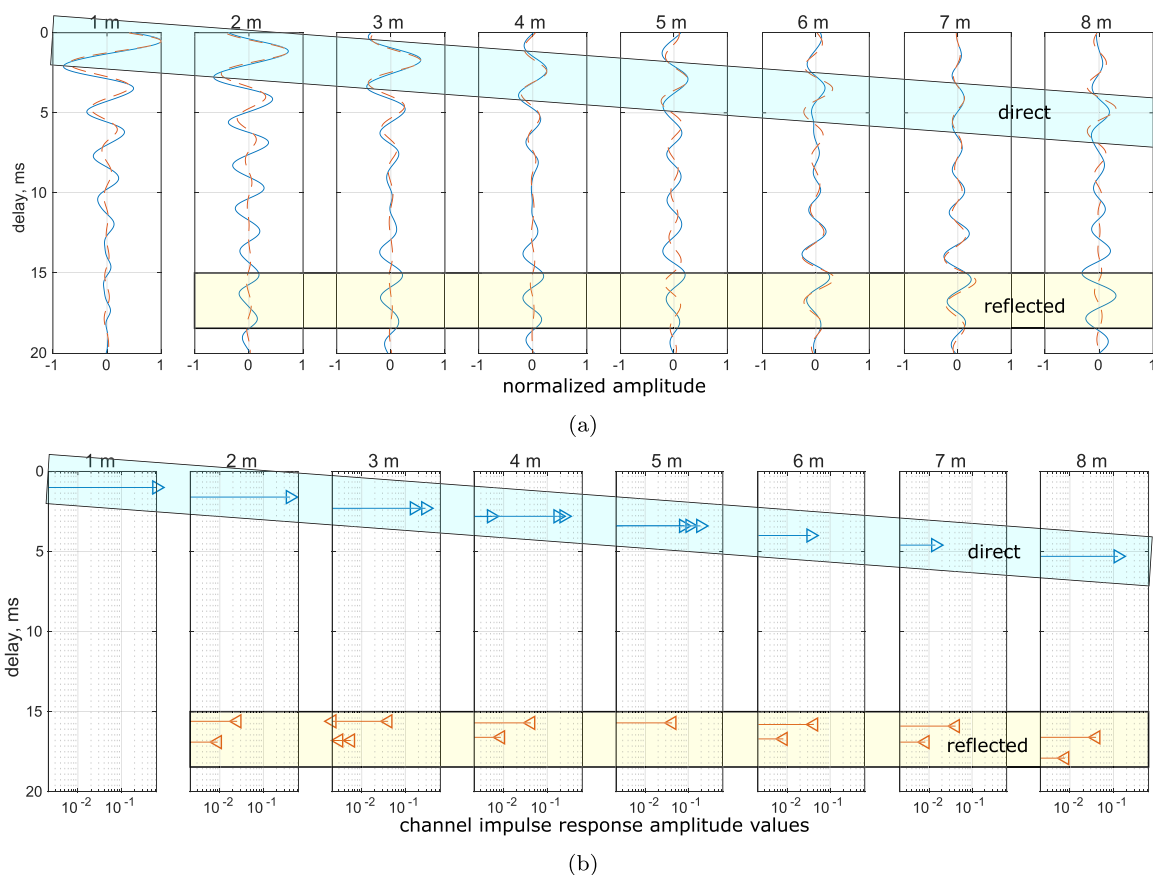


**Fig. 5.** Observations and modelled impulse response at different distances from the CO<sub>2</sub> seep site. (a) Observed sound field at different offsets (blue) and matched synthetic trace (red). The amplitude at each distance is normalised to the peak value in the cross-correlation at an offset of 1 m. (b) Impulse response derived from ray-tracing used to produce the synthetic. The direct arrivals are indicated within the blue box, while the arrival that results from a reflection at the water-surface is within the yellow box. (For interpretation of the references to colour in this figure legend, the reader is referred to the web version of this article.)

**Table 1**

Bubble sound propagation and range estimation from average delays estimated by cross-correlation between the transect data (1–8 m) and the reflected data measured at  $-0.3$  m. Propagation multipath include direct path and sea surface reflected path.

Transect	Path	Delay	Length	Error
1 m with $-0.3$ m	Direct	0.47 ms	0.70 m	2.9%
	reflect	16.29 ms	24.44 m	
2 m with $-0.3$ m	Direct	1.06 ms	1.60 m	3.2%
	reflect	16.54 ms	24.81 m	
3 m with $-0.3$ m	Direct	1.74 ms	2.63 m	6.4%
	reflect	16.56 ms	24.84 m	
4 m with $-0.3$ m	Direct	2.24 ms	3.38 m	5.9%
	reflect	16.56 ms	24.84 m	
5 m with $-0.3$ m	Direct	2.83 ms	4.28 m	3.8%
	reflect	16.63 ms	24.94 m	
6 m with $-0.3$ m	Direct	3.49 ms	5.27 m	6.7%
	reflect	16.69 ms	25.03 m	
7 m with $-0.3$ m	Direct	4.02 ms	6.07 m	3.8%
	reflect	16.78 ms	25.17 m	
8 m with $-0.3$ m	Direct	4.82 ms	7.28 m	4.3%
	reflect	17.84 ms	26.76 m	

at some part of low-frequency spectrum were not measured, shown as weak PSD in the dashed circles, which is due to the interference from Lloyd's mirror effect. This has been incorporated in the analysis by considering the multipath propagation using the channel impulse response derived equivalent range to replace the physical range for each transect.

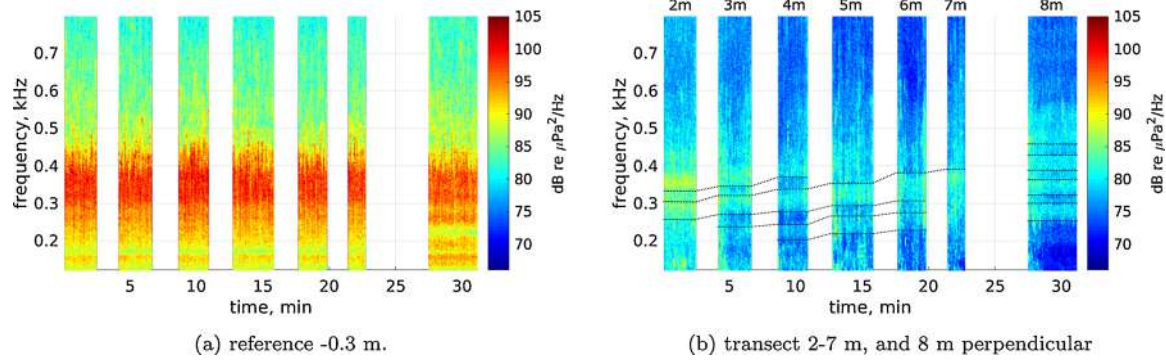
### 3.3. Gas flux and bubble size

The gas flux and CO<sub>2</sub> bubble size distribution were quantified by passive acoustic inversion. The time taken for the CO<sub>2</sub> to fill a 2-L plastic measuring cylinder was used to directly determine the gas flux from our studied seep site. Repeated measurements by divers allowed an average fill time of 53 seconds to be determined, which equates to a flux rate of 2.3 L/min (Fig. 8(a)).

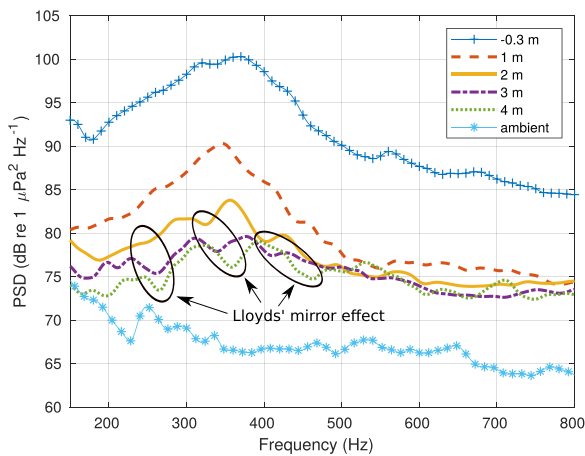
#### 3.3.1. Gas flux determination

Fig. 9 shows the two examples (4 and 7 m) of output of the Bellhop ray-tracing model for the east to west bubble transect. Both the direct (blue) and reflected (red) path for the two cases are visible, while the path with both the reflection from the sea surface and seabed are shown in black colour lines. Fig. 5(b) shows the modelled channel impulse response as a function of deployment distance. The impulse responses with delay less than 10 ms correspond to the direct path, while those above 10 ms correspond to the propagation path reflected from the sea surface. The impulse response delays match well with the cross-correlation results from the measured acoustic data shown in Fig. 5(a) blue line peaks boxed and in Table 1.

We further use the bubble forward model to generate modelled bubble sound and calculate the modelled cross-correlation results for comparison with the measured one. The comparison results are shown in Fig. 5(a) red lines. It is seen that the two lines match quite well, particularly at 1–4 and 6–7 m where the direct path or reflected dominates the propagation. While at 5 m and perpendicular 8 m where the signals' strength from the two path are comparable resulting significant interference from the Lloyd's mirror effect. Unmatched part of the



**Fig. 6.** Spectrograms from measured hydrophone data. (a) shows the frequency interval of interest 150–800 Hz; (b) shows the outline of Lloyd's mirror effect which can be observed from the spectrum marked as dashed lines. Recorded sound with noise introduced by divers conducting the hydrophone transect has been removed and is shown as blank in the figures.



**Fig. 7.** Power spectral density (PSD) of the sound recorded at different distances from the CO<sub>2</sub> seep site. Frequencies between 150 and 800 Hz record bubble sounds, with sound level decreasing with distance from the seep. The solid circles indicate distances and frequencies affected by the Lloyd's mirror effect. The PSD at transect 4 m is measured as ~10 dB higher than that of the ambient noise.

correlation curve can be partly interpreted to the multiple interference bubble streams around the measured focused seep site in the experiment while a single bubble seep is considered in the model.

As we have the impulse responses for the transect obtained from the ray tracing, we can model the signal at the hydrophones by convolving the signals measured at the reference position with the impulse

responses (Henson et al., 2014). The frequency spectrum is quite weak from the modelling at distances 5–8 m bubble transect due to the significant attenuation as shown in Fig. 4(b), which does not match the observations as shown in Fig. 6(b). This is because the level of focused seepage sound at such greater transect distances was less than 10 dB above the ambient environment noise level, and the level of interference sound from other bubble streams was increased. Thus here we are unable to determine the focus bubble gas flux at distance 5–8 m, where the measured acoustic sound was severely influenced by the noise interference.

The comparisons between the gas flux determination from passive acoustic inversion using spherical spreading range and multipath equivalent range are shown in Table 2. It is seen that the error of gas flux estimation from inversion with spherical spreading is most accurate close to the seep location, with errors up to 41% at other ranges. The accuracy increases significantly when the effects of multipath are included. Taken together, we successfully estimated the gas flux using the inversion method with relatively small errors (< 10%) for ranges up to 4 m.

### 3.3.2. Bubble size determination

Fig. 10 shows the PDF of the estimated bubble size distribution from passive acoustic inversion at ranges from -0.3 to 4 m. The radius of CO<sub>2</sub> bubbles emerging from the 12.5 m deep seafloor were mainly between 1 and 2.5 cm. Estimated bubble size tends to decrease as the hydrophone ranges increase. The increase in the number of estimated small bubbles with radius less than 1.3 cm is due to the reduced signal to noise ratio in this band, where some of the ambient noise is incorporated with the noise of bubbles being emitted from the seep. The

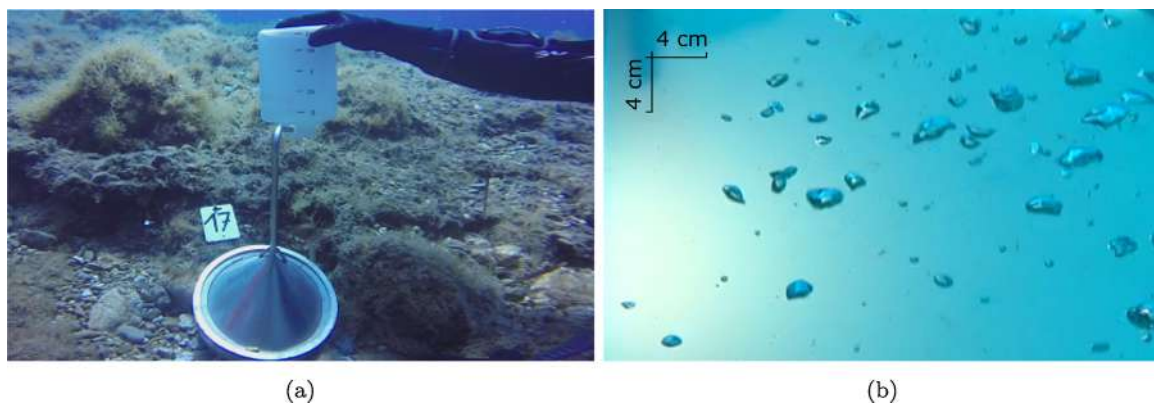


**Fig. 8.** Experimental scenarios. (a) Gas Bubbles at the vent site investigated filled a two-litre container in 53 s, resulting in an average flow rate of 2.3 L/min. (b) Bubble size measurement using underwater camera. The background whiteboard was 18 × 30 cm in dimension. The distance between the camera and the whiteboard was 1.4 m. The bubble stream was rising ± 20 cm mid-way between the camera and the whiteboard.

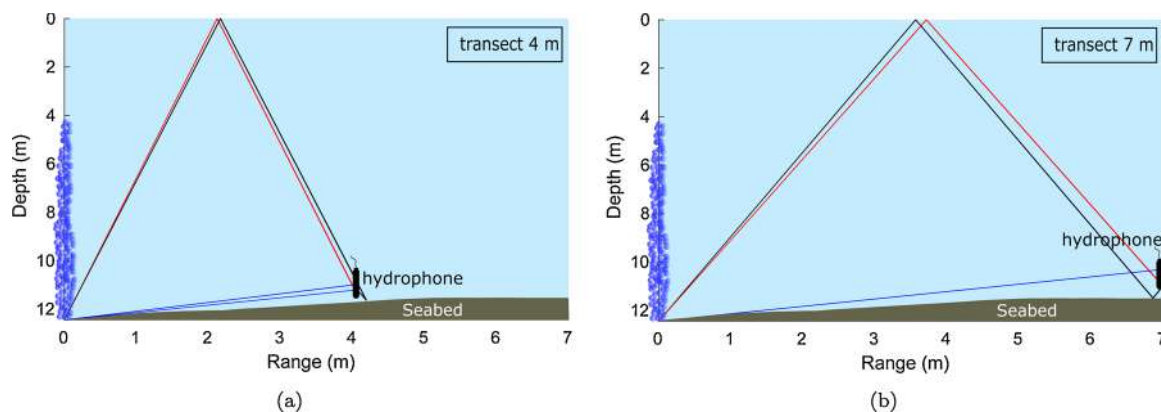


**Fig. 9.** Examples of Bellhop ray-trace output for the bubble transect over the west side of Bottaro Crater. (a) Transect range 4 m; (b) transect range 7 m. Both cases show the direct path, the path with only sea surface reflection, and the path with both sea surface and seabed reflection. Black ray hits both boundaries; red ray hits surface only; and blue ray hits bottom only. (For interpretation of the references to colour in this figure legend, the reader is referred to the web version of this article.)

**Table 2**

Comparison of gas flux estimation results from passive acoustic inversion considering spherical spreading and channel multipath propagation. The diver measured gas flow rate from *in situ* collection is 2.3 L/min.

Field range	Spherical		Multipath	
	Flow rate	Error	Flow rate	Error
-0.3 m	2.2 L/min	4.40%	2.4 L/min	7.1%
1 m	1.8 L/min	18.6%	2.1 L/min	6.2%
2 m	1.3 L/min	40.7%	2.3 L/min	0.0%
3 m	1.5 L/min	32.7%	2.4 L/min	7.1%
4 m	1.7 L/min	23.0%	2.5 L/min	8.8%

resulting uncertainties are interpreted to be the combination of bubble acoustic attenuation in the channel, the Lloyd's mirror effect and the presence of ambient noise. As the seep/hydrophone distance increases, the frequency band from the Lloyd's mirror effect also shifts, which changes the estimated bubble size.

Fig. 8(b) shows a horizontal view of the bubble plume, which shows that the radius of majority bubbles were normally between 1 and 2.5 cm. This provides agreement between the modelled and measured bubble size and proves the effectiveness of our approach.

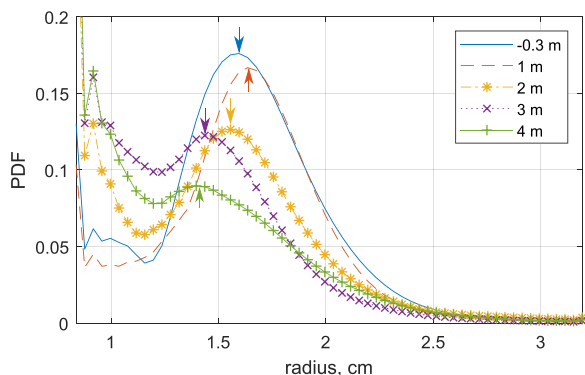


**Fig. 10.** Probability density function (PDF) of the estimated bubble size distribution from passive acoustic inversion at different distances from the CO<sub>2</sub> seep site. Estimated bubble size tends to decrease as the hydrophone ranges increases (peak moves from 1.7 cm (at 1 m) to 1.4 cm (at 4 m) as indicated by arrows). The increase in the number of small bubbles with radius less than 1.3 cm is due to the reduced SNR at greater ranges.

**4. Conclusions and discussion**

The ability of passive acoustic monitoring to detect and quantify continuous natural CO<sub>2</sub> gas leakage from sub-seabed was tested at different ranges in shallow water offshore Panarea island. A CO<sub>2</sub> bubble plume was successfully detected at ranges up to 8 m, and the gas flux and bubble size determined for distances of up to 4 m, where the bubble sound pressure is measured as ~10 dB higher than that of the ambient noise. The Panarea passive acoustic tests have demonstrated that the passive acoustic inversion method described here, when integrated with scenario modelling is an appropriate and cost-effective approach to be applied in detection and quantification of seabed gas leakage in shallow water.

In particular, the transect data has enabled a definition of multipath propagation (direct or sea surface reflect) of bubble sound in the acoustic channel, and has been used to estimate the gas flux and bubble size distribution. The range at which bubbles can be detected has been limited by multipath propagation, significant attenuation, and interference in underwater acoustic channels. The estimated gas fluxes show agreement within 10% error to the measured gas fluxes, and the estimated bubble sizes are comparable to those observed.

Modelling based on a ray-tracing program considers the multipath propagation, providing relatively accurate equivalent range for gas flux determination up to 4 m in the shallow water scenario investigated. However, there were multiple other bubble seeps around the bubble transect area which increased the sound levels and made the determination of gas flux beyond 4 m for a specific bubble seep unsuccessful. Characterisations of the site-specific source-receiver geometry, bathymetry, bubble plume shape/angle, sediment properties, and sound speed profile are also important before conducting passive acoustic monitoring and are of particular importance when designing monitoring strategies for offshore CCS sites.

The study area at Panarea is in shallower water (12.5 m) than sites normally considered for CCS across the Global Ocean (e.g., Zhou et al., 2018; Strachan et al., 2011; Claprod et al., 2012; Teatini et al., 2014; Chadwick et al., 2019; Chadwick, 2015; Shell, 2017), which are in deeper shelf seas. We can still apply the passive acoustic techniques developed here for bubble detection and quantification in deeper water. The applicable range of such detection and quantification depends of the actual gas flux on the seepage site, the depth of the water, and the ambient noise in the area. The gas flux in this study was 2.3 L/min which results in a detection range up to 8 m and a quantification range up to 4 m. Considering the same ambient noise level and the same emergent gas flux in deeper water, due to the high propagation loss (about 40 dB from the seabed to the sea surface (Li et al., 2019b)) in the acoustic channel, only the direct acoustic path for the bubble sound



would need to be considered, simplifying the analysis. Our methods will be applicable in the deep sea, and for normal ambient noise levels we should be able to detect and quantify sound at greater offset ranges than at Panarea. We are currently analysing data from the STEMM-CCS experiment (<https://www.stemm-ccs.eu/>) in the central North Sea, which included a passive acoustic component, and will be the subject of future publications.

Passive acoustic recorders fixed to the seabed can be linked to battery packs to permit long-period (greater than a year) deployments. The requirement for relatively high sampling rates to record the bubble sounds with sufficient fidelity, means that data volumes are large, and there is no straightforward method to remotely transmit the data without direct cabling; the data is retrieved when the acoustic recorder is recovered. In practical terms the relatively short offset detection ranges for bubble sounds on hydrophones, means that fixed passive acoustic recorders on the seabed will only be deployed at sites where there is high risk of gas escape (e.g., seabed installations including abandoned oil and gas wells), or after detection by active acoustic sensors. Additional methods for passive acoustic sensing include deployment on autonomous underwater vehicles, and using distributed acoustic sensing, and both these techniques are the subject of continuing work.

### Conflict of interest

None declared.

### Acknowledgements

Funding was provided by the European Union Horizon 2020 research and innovation programme under the grant agreement number 654462 (STEMM-CCS). We thank the scientific divers Andrea Fogliozzi and Martina Gaglioti for their professional and tireless work.

### References

- Ainslie, M.A., Leighton, T.G., 2009. Near resonant bubble acoustic cross-section corrections, including examples from oceanography, volcanology, and biomedical ultrasound. *J. Acoust. Soc. Am.* 126 (5), 2163–2175. <https://doi.org/10.1121/1.3180130>.
- Aliani, S., Bortoluzzi, G., Caramanna, G., Raffa, F., 2010. Seawater dynamics and environmental settings after November 2002 gas eruption off Bottaro (Panarea, Aeolian Islands, Mediterranean Sea). *Cont. Shelf Res.* 30 (12), 1338–1348. <https://doi.org/10.1016/j.csr.2010.04.016>.
- Anzidei, M., Esposito, A., Bortoluzzi, G., De Giosa, F., 2005. The high resolution bathymetric map of the exhalative area of Panarea (Aeolian Islands, Italy). *Ann. Geophys.* 48 (6). <https://doi.org/10.4401/ag-3242>.
- Atamanchuk, D., Tengberg, A., Aleynik, D., Fietzek, P., Shitashima, K., Lichtschlag, A., Hall, P.O., Stahl, H., 2015. Detection of CO<sub>2</sub> leakage from a simulated sub-seabed storage site using three different types of pCO<sub>2</sub> sensors. *Int. J. Greenhouse Gas Control* 38, 121–134. <https://doi.org/10.1016/j.ijggc.2014.10.021>.
- Beccaluna, L., Gabbianelli, G., Lucchini, F., Rossi, P., Savelli, C., 1985. Petrology and K/Ar ages of volcanics dredged from the Eolian seamounts: implications for geodynamic evolution of the southern Tyrrhenian basin. *Earth Planet. Sci. Lett.* 74 (2–3), 187–208. [https://doi.org/10.1016/0012-821X\(85\)90021-4](https://doi.org/10.1016/0012-821X(85)90021-4).
- Bergès, B.J., Leighton, T.G., White, P.R., 2015. Passive acoustic quantification of gas fluxes during controlled gas release experiments. *Int. J. Greenhouse Gas Control* 38, 64–79. <https://doi.org/10.1016/j.ijggc.2015.02.008>.
- Blackford, J., Bull, J.M., Cevatoglu, M., Connelly, D., Hauton, C., James, R.H., Lichtschlag, A., Stahl, H., Widdicombe, S., Wright, I.C., 2015. Marine baseline and monitoring strategies for carbon dioxide capture and storage (CCS). *Int. J. Greenhouse Gas Control* 38, 221–229. <https://doi.org/10.1016/j.ijggc.2014.10.004>.
- Calanchi, N., Capaccioni, B., Martini, M., Tassi, F., Valentini, L., 1995. Submarine gas-emission from Panarea Island (Aeolian Archipelago): distribution of inorganic and organic compounds. *Acta Vulcanol.* 7 (1), 43–48.
- Caracausi, A., Ditta, M., Italiano, F., Longo, M., Nuccio, P., Paonita, A., Rizzo, A., 2005. Changes in fluid geochemistry and physico-chemical conditions of geothermal systems caused by magmatic input: the recent abrupt outgassing off the island of Panarea (Aeolian Islands, Italy). *Geochim. Cosmochim. Acta* 69 (12), 3045–3059. <https://doi.org/10.1016/j.gca.2005.02.011>.
- Caramanna, G., Fietzek, P., Maroto-Valer, M., 2011. Monitoring techniques of a natural analogue for sub-seabed CO<sub>2</sub> leakages. *Energy Proc.* 4, 3262–3268. <https://doi.org/10.1016/j.egypro.2011.02.245>.
- Caramanna, G., Wei, Y., Maroto-Valer, M.M., Nathanail, P., Steven, M., 2013. Laboratory experiments and field study for the detection and monitoring of potential seepage from CO<sub>2</sub> storage sites. *Appl. Geochem.* 30, 105–113. <https://doi.org/10.1016/j.egypro.2013.06.229>.
- Caserini, S., Dolci, G., Azzellino, A., Lanfredi, C., Rigamonti, L., Barreto, B., Grosso, M., 2017. Evaluation of a new technology for carbon dioxide submarine storage in glass capsules. *Int. J. Greenhouse Gas Control* 60, 140–155. <https://doi.org/10.1016/j.ijggc.2017.03.007>.
- Cevatoglu, M., Bull, J.M., Vardy, M.E., Gernon, T.M., Wright, I.C., Long, D., 2015. Gas migration pathways, controlling mechanisms and changes in sediment acoustic properties observed in a controlled sub-seabed CO<sub>2</sub> release experiment. *Int. J. Greenhouse Gas Control* 38, 26–43. <https://doi.org/10.1016/j.ijggc.2015.03.005>.
- Chadwick, R., Williams, G., Falcon-Suarez, I., 2019. Forensic mapping of seismic velocity heterogeneity in a CO<sub>2</sub> layer at the Sleipner CO<sub>2</sub> storage operation, North Sea, using time-lapse seismics. *Int. J. Greenhouse Gas Control* 90, 102793. <https://doi.org/10.1016/j.ijggc.2019.102793>.
- Chadwick, A., 2015. Review Confirms Goldeneye Storage Capability and Capacity, Tech. Rep. 1. British Geological Survey. [https://www.bgs.ac.uk/news/docs/Goldeneye\\_CO2\\_storage\\_Press\\_Release.pdf](https://www.bgs.ac.uk/news/docs/Goldeneye_CO2_storage_Press_Release.pdf).
- Chiodini, G., Caliro, S., Caramanna, G., Granieri, D., Minopoli, C., Moretti, R., Perotta, L., Ventura, G., 2006. Geochemistry of the submarine gaseous emissions of Panarea (Aeolian Islands, Southern Italy): magmatic vs. hydrothermal origin and implications for volcanic surveillance. *Pure Applied Geophys.* 163 (4), 759–780. <https://doi.org/10.1007/s00024-006-0037-y>.
- Claproot, M., Gloaguen, E., Giroux, B., Konstantinovskaya, E., Malo, M., Duchesne, M.J., 2012. Workflow using sparse vintage data for building a first geological and reservoir model for CO<sub>2</sub> geological storage in deep saline aquifer. A case study in the St. Lawrence Platform, Canada. *Greenhouse Gases: Sci. Technol.* 2 (4), 260–278. <https://doi.org/10.1002/ghg.1292>.
- Dekov, V.M., Savelli, C., 2004. Hydrothermal activity in the SE Tyrrhenian Sea: an overview of 30 years of research. *Marine Geol.* 204 (1–2), 161–185. [https://doi.org/10.1016/S0025-3227\(03\)00355-4](https://doi.org/10.1016/S0025-3227(03)00355-4).
- Esposito, A., Giordano, G., Anzidei, M., 2006. The 2002–2003 submarine gas eruption at Panarea volcano (Aeolian Islands, Italy): volcanology of the seafloor and implications for the hazard scenario. *Marine Geol.* 227 (1–2), 119–134. <https://doi.org/10.1016/j.margeo.2005.11.007>.
- Gabbianelli, G., Gillot, P., Lanzafame, G., Romagnoli, C., Rossi, P., 1990. Tectonic and volcanic evolution of Panarea (Aeolian islands, Italy). *Mar. Geol.* 92 (3–4), 313–326. [https://doi.org/10.1016/0025-3227\(90\)90011-8](https://doi.org/10.1016/0025-3227(90)90011-8).
- Gerstein, E.R., 2002. Manatees, bioacoustics and boats: hearing tests, environmental measurements and acoustic phenomena may together explain why boats and animals collide. *Am. Sci.* 90 (2), 154–163.
- Graziani, S., Beaubien, S.E., Bigi, S., Lombardi, S., 2014. Spatial and temporal pCO<sub>2</sub> marine monitoring near Panarea Island (Italy) using multiple low-cost GasPro sensors. *Environ. Sci. Technol.* 48 (20), 12126–12133. <https://doi.org/10.1021/es500666u>.
- Henson, B., Li, J., Zakharov, Y.V., Liu, C., 2014. Waymark baseband underwater acoustic propagation model. *IEEE Underwater Communications and Networking (UComms)* 1–5. <https://doi.org/10.1109/UComms.2014.7017132>.
- Hvidevold, H.K., Alendal, G., Johannessen, T., Ali, A., 2016. Survey strategies to quantify and optimize detecting probability of a CO<sub>2</sub> seep in a varying marine environment. *Environ. Modell. Softw.* 83, 303–309. <https://doi.org/10.1016/j.envsoft.2016.06.006>.
- Italiano, F., Nuccio, P., 1991. Geochemical investigations of submarine volcanic exhalations to the east of Panarea, Aeolian Islands, Italy. *J. Volcanol. Geotherm. Res.* 46 (1–2), 125–141. [https://doi.org/10.1016/0377-0273\(91\)90079-F](https://doi.org/10.1016/0377-0273(91)90079-F).
- Italiano, F., Mauerer, R., Mastroli, A., Heinicke, J., 2011. SMM, a new seafloor monitoring module for real-time data transmission: an application to shallow hydrothermal vents. *Proc. Earth Planet. Sci.* 4, 93–98. <https://doi.org/10.1016/j.proeps.2011.11.010>.
- Jackson, D., Richardson, M., 2007. *High-Frequency Seafloor Acoustics*. Springer Science & Business Media.
- Kirk, K., 2011. *Natural CO<sub>2</sub> flux literature review for the QICS project, British Geological Survey Commissioned Report*. *Compt. Rendus Geosci.* 11.
- Kita, J., Stahl, H., Hayashi, M., Green, T., Watanabe, Y., Widdicombe, S., 2015. Benthic megafauna and CO<sub>2</sub> bubble dynamics observed by underwater photography during a controlled sub-seabed release of CO<sub>2</sub>. *Int. J. Greenhouse Gas Control* 38, 202–209. <https://doi.org/10.1016/j.ijggc.2014.11.012>.
- Kolster, C., Agada, S., Mac Dowell, N., Krevor, S., 2018. The impact of time-varying CO<sub>2</sub> injection rate on large scale storage in the UK Bunter Sandstone. *Int. J. Greenhouse Gas Control* 68, 77–85. <https://doi.org/10.1016/j.ijggc.2017.10.011>.
- Leblond, L., Scalabrin, C., Berger, L., 2014. Acoustic monitoring of gas emissions from the seafloor. Part I: quantifying the volumetric flow of bubbles. *Mar. Geophys. Res.* 35 (3), 191–210. <https://doi.org/10.1007/s11001-014-9223-y>.
- Leifer, I., MacDonald, I., 2003. Dynamics of the gas flux from shallow gas hydrate deposits: interaction between oily hydrate bubbles and the oceanic environment. *Earth Planet. Sci. Lett.* 210 (3), 411–424. [https://doi.org/10.1016/S0012-821X\(03\)00173-0](https://doi.org/10.1016/S0012-821X(03)00173-0).
- Leighton, T., White, P., 2011. Quantification of undersea gas leaks from carbon capture and storage facilities, from pipelines and from methane seeps, by their acoustic emissions. *Proc. R. Soc. A*. <https://doi.org/10.1098/rspa.2011.0221>.
- Leighton, T.G., 1994. *The Acoustic Bubble*. <https://doi.org/10.1017/S0022112094214519>. ISBN: 0-12-44190-8.
- Li, J., Zakharov, Y.V., 2018. Efficient use of space-time clustering for underwater acoustic communications. *IEEE J. Ocean. Eng.* 43 (1), 173–183. <https://doi.org/10.1109/JOE.2017.2688558>.
- Li, J., Liao, L., Zakharov, Y.V., 2016. Space-time cluster combining for UWA communications. *OCEANS 2016 – Shanghai* 1–6. <https://doi.org/10.1109/OCEANSAP.2016.7485344>.
- Li, J., Zakharov, Y.V., Henson, B., 2018. Multibranch autocorrelation method for Doppler

- estimation in underwater acoustic channels. *IEEE J. Ocean. Eng.* 43 (4), 1099–1113. <https://doi.org/10.1109/JOE.2017.2761478>.
- Li, J., White, P.R., Roche, B., Bull, J.M., Davis J.W., Leighton, T.G., Deponte, M., Gordini, E., Cotterle, D., 2019a. Natural seabed gas leakage – variability imposed by tidal cycles. *MTS/IEEE OCEANS 2019 – Seattle, USA* 1–6.
- Li, J., White, P.R., Bull, J.M., Leighton, T.G., 2019b. A noise impact assessment model for passive acoustic measurements of seabed gas fluxes. *Ocean Eng.* 183 (1), 294–304. <https://doi.org/10.1016/j.oceaneng.2019.03.046>.
- Li, J., White, P.R., Bull, J.M., Leighton, T.G., Roche, B., 2019c. A model for variations of sound speed and attenuation from seabed gas emissions. *MTS/IEEE OCEANS 2019 – Seattle, USA* 1–9.
- Li, J., 2017. DOA tracking in time-varying underwater acoustic communication channels. *MTS/IEEE OCEANS 2017 – Aberdeen* 1–9. <https://doi.org/10.1109/OCEANSE.2017.8084563>.
- Loewen, M., Melville, W., 1991. A model of the sound generated by breaking waves. *J. Acoust. Soc. Am.* 90 (4), 2075–2080. <https://doi.org/10.1121/1.401634>.
- Lucchi, F., Tranne, C., Calanchi, N., Rossi, P., Keller, J., 2007. The stratigraphic role of marine deposits in the geological evolution of the Panarea volcano (Aeolian Islands, Italy). *J. Geol. Soc.* 164 (5), 983–996. <https://doi.org/10.1144/0016-76492006-135>.
- Lupton, J., de Ronde, C., Sprovieri, M., Baker, E.T., Bruno, P.P., Italiano, F., Walker, S., Faure, K., Leybourne, M., Britten, K., et al., 2011. Active hydrothermal discharge on the submarine Aeolian Arc. *J. Geophys. Res.: Solid Earth* 116 (B2). <https://doi.org/10.1029/2010JB007738>.
- Mabon, L., Shackley, S., Bower-Bir, N., 2014. Perceptions of sub-seabed carbon dioxide storage in Scotland and implications for policy: a qualitative study. *Mar. Policy* 45, 9–15. <https://doi.org/10.1016/j.marpol.2013.11.011>.
- Pachauri, R.K., Allen, M.R., Barros, V.R., Broome, J., Cramer, W., Christ, R., Church, J.A., Clarke, L., Dahe, Q., Dasgupta, P., et al., 2014. Climate change 2014: synthesis report. Contribution of Working Groups I, II and III to the Fifth Assessment Report of the Intergovernmental Panel on Climate Change.
- Porter, M.B., 2011. *The Bellhop Manual and User's Guide: Preliminary Draft*. Tech. Rep. Heat, Light, and Sound Research, Inc., La Jolla, CA, USA.
- Roelofse, C., Alves, T.M., Gafeira, J., Kamaldeen, O.O., 2019. An integrated geological and GIS-based method to assess caprock risk in mature basins proposed for carbon capture and storage. *Int. J. Greenhouse Gas Control* 80, 103–122. <https://doi.org/10.1016/j.ijggc.2018.11.007>.
- Schmidt, M., Linke, P., Sommer, S., Esser, D., Cherednichenko, S., 2015. Natural CO<sub>2</sub> seeps offshore Panarea: a test site for subsea CO<sub>2</sub> leak detection technology. *Mar. Technol. Soc. J.* 49 (1), 19–30. <https://doi.org/10.4031/MTSJ.49.1.3>.
- Shell, 2017. Goldeneye Gas Platform, United Kingdom. <http://www.offshore-technology.com/projects/goldeneye/>.
- Shitashima, K., Maeda, Y., Sakamoto, A., 2015. Detection and monitoring of leaked CO<sub>2</sub> through sediment, water column and atmosphere in a sub-seabed CCS experiment. *Int. J. Greenhouse Gas Control* 38, 135–142. <https://doi.org/10.1016/j.ijggc.2014.12.011>.
- Siedler, G., Peters, H., 1986. Properties of sea water. *Oceanography* 233–264.
- Stork, A.L., Allmark, C., Curtis, A., Kendall, J.-M., White, D.J., 2018. Assessing the potential to use repeated ambient noise seismic tomography to detect CO<sub>2</sub> leaks: application to the Aquistore storage site. *Int. J. Greenhouse Gas Control* 71, 20–35. <https://doi.org/10.1016/j.ijggc.2018.02.007>.
- Strachan, N., Hoefnagels, R., Ramirez, A., Van den Broek, M., Fidje, A., Espegren, K., Seljom, P., Bles, M., Kober, T., Grohnheit, P.E., 2011. CCS in the North Sea region: a comparison on the cost-effectiveness of storing CO<sub>2</sub> in the Utsira formation at regional and national scales. *Int. J. Greenhouse Gas Control* 5 (6), 1517–1532. <https://doi.org/10.1016/j.ijggc.2011.08.009>.
- Strasberg, M., 1956. Gas bubbles as sources of sound in liquids. *J. Acoust. Soc. Am.* 28 (1), 20–26. <https://doi.org/10.1121/1.1908212>.
- Taylor, P., Stahl, H., Vardy, M.E., Bull, J.M., Akhurst, M., Hauton, C., James, R.H., Lichtschlag, A., Long, D., Aleynik, D., et al., 2015. A novel sub-seabed CO<sub>2</sub> release experiment informing monitoring and impact assessment for geological carbon storage. *Int. J. Greenhouse Gas Control* 38, 3–17. <https://doi.org/10.1016/j.ijggc.2014.09.007>.
- Teatini, P., Castelletto, N., Gambolati, G., 2014. 3D geomechanical modeling for CO<sub>2</sub> geological storage in faulted formations. a case study in an offshore northern Adriatic reservoir, Italy. *Int. J. Greenhouse Gas Control* 22, 63–76. <https://doi.org/10.1016/j.ijggc.2013.12.021>.
- Veloso, M., Greinert, J., Mienert, J., Batist, M.D., 2015. A new methodology for quantifying bubble flow rates in deep water using splitbeam echosounders: examples from the Arctic offshore NW-Svalbard. *Limnol. Oceanogr.: Methods* 13 (6), 267–287. <https://doi.org/10.1002/lom3.10024>.
- Vielstädte, L., Linke, P., Schmidt, M., Sommer, S., Haeckel, M., Braack, M., Wallmann, K., 2019. Footprint and detectability of a well leaking CO<sub>2</sub> in the Central North Sea: implications from a field experiment and numerical modelling. *Int. J. Greenhouse Gas Control* 84, 190–203. <https://doi.org/10.1016/j.ijggc.2019.03.012>.
- von Deimling, J.S., Linke, P., Schmidt, M., Rehder, G., 2015. Ongoing methane discharge at well site 22/4b (North Sea) and discovery of a spiral vortex bubble plume motion. *Mar. Petrol. Geol.* 68, 718–730. <https://doi.org/10.1016/j.marpetgeo.2015.07.026>.
- Zhou, D., Li, P., Liang, X., Liu, M., Wang, L., 2018. A long-term strategic plan of offshore CO<sub>2</sub> transport and storage in northern South China Sea for a low-carbon development in Guangdong province, China. *Int. J. Greenhouse Gas Control* 70, 76–87. <https://doi.org/10.1016/j.ijggc.2018.01.011>.